ADVANCED FUNCTIONAL MATERIALS
www.afm-journal.de

Multi-Frequency Ultrasound Directed Self-Assembly

*Christopher Tre Presley, Fernando Guevara Vasquez, and Bart Raeymaekers**

Ultrasound-directed self-assembly (DSA) utilizes the acoustic radiation force associated with a standing ultrasound wave field to organize particles dispersed in a fluid medium into specific patterns. State-of-the-art ultrasound DSA methods use single-frequency ultrasound wave fields, which only allow organizing particles into simple, periodic patterns, or require a large number of ultrasound transducers to assemble complex patterns. In contrast, this work introduces multi-frequency ultrasound wave fields to organize particles into complex patterns. A method is theoretically derived to determine the operating parameters (frequency, amplitude, phase) of any arrangement of ultrasound transducers, required to assemble spherical particles dispersed in a fluid medium into specific patterns, and experimentally validated for a system with two frequencies. The results show that multi-frequency compared to single-frequency ultrasound DSA enables the assembly of complex patterns of particles with substantially fewer ultrasound transducers. Additionally, the method does not incur a penalty in terms of accuracy, and it does not require custom hardware for each different pattern, thus offering reconfigurability, which contrasts, e.g., acoustic holography. Multi-frequency ultrasound DSA can spur progress in a myriad of engineering applications, including the manufacturing of multi-functional polymer matrix composite materials that derive their structural, electric, acoustic, or thermal properties from the spatial organization of particles in the matrix.

1. Introduction

Directed self-assembly (DSA) is a process by which particles or other discrete components dispersed in a fluid medium organize as a result of interactions between the components themselves and/or with their environment.[1] External field DSA techniques employ a set of transducers to establish an electric,[2] magnetic,[3] or ultrasound wave[4] field, which organizes and orients the particles into specific patterns. Tuning the operating parameters of the transducers changes the field, which in turn modifies the organization and orientation of the particles. Electric and magnetic fields enable organizing and orienting (high-aspect ratio) particles into specific patterns, but require electrically conductive or magnetic particles, respectively, and require ultra-high field strengths (e.g., 500 V[5] and 80kOe),[6] which typically limit dimensional scalability to micrometer or millimeter scale areas. Coupled-fields have also been used to organize particles into specific patterns.[7] Ultrasound DSA on the other hand relies on the acoustic radiation force associated with a standing ultrasound wave field to organize and orient particles into specific patterns. The existence of the acoustic radiation force only depends on the acoustic contrast between the particles and the fluid medium, which derives from their density and compressibility.[8] Hence, material choice is almost unlimited and includes organic and inorganic particles.[9–12] Furthermore, scalability is only limited by the attenuation of the ultrasound waves in the fluid medium, which primarily depends on the frequency of the ultrasound wave field and the viscosity of the medium.[13] As a result, ultrasound wave fields improve on the material choice and scalability limitations that electric and magnetic fields impose during external field DSA.

Theoretical studies of the acoustic radiation force of incompressible spherical particles suspended in an inviscid fluid began with King in the 1930s.[14] Subsequently, Yosioka and Kawasima considered compressible spherical particles in an inviscid fluid.[15] Gor'kov unified different theories, and formulated a generalized acoustic radiation force theory for compressible spherical particles smaller than the acoustic wavelength, dispersed in an inviscid fluid medium.[9]

Ultrasound DSA reduces to solving a forward problem to determine the organization and orientation of particles that result from tuning the operating parameters of a set of ultrasound transducers (frequency, amplitude, and phase), and an inverse problem to calculate the operating parameters of a set of ultrasound transducers required to organize and orient particles into a specific pattern. The literature documents theoretical solutions to both the forward and inverse problems for spherical particles

C. T. Presley, B. Raeymaekers
Department of Mechanical Engineering
Virginia Tech
Blacksburg, VA 24061, USA
E-mail: bart.raeymaekers@vt.edu
F. Guevara Vasquez
Department of Mathematics
University of Utah
Salt Lake City, UT 84112, USA

The ORCID identification number(s) for the author(s) of this article can be found under https://doi.org/10.1002/adfm.202400193

DOI: 10.1002/adfm.202400193

(e.g., polystyrene, carbon, aluminum, glass) in 1D,[16] 2D,[17–19] and 3D,[20–23] and for high-aspect ratio particles in 2D[24] and 3D,[25] mostly in low-viscosity media (e.g., water, air), but some publications also show experiments in viscous media (e.g., thermoset resin, polymer binder, photopolymer, and gels).[10,26,27]

Settnes and Bruus[28] expanded Gor'kov's acoustic radiation force theory from inviscid to viscous media and showed that the amplitude of the acoustic radiation force depends on the medium viscosity. Using this viscous theory, Noparast et al.[29] demonstrated that the locations where particles organize depend on the viscosity of the medium because the sound propagation velocity and, thus, the wavelength of the ultrasound wave, is a function of the viscosity. However, the differences between locations where particles assemble in viscous and inviscid media are small, because the sound propagation velocity of water $c_m = 1500$ ms^{-1} (inviscid medium) is similar to that of viscous liquids, e.g. oils, or (photo)polymer resins $1300 \leq c_m \leq 1400$ ms^{-1}. Hence, inviscid theory is often used in conjunction with ultrasound DSA experiments in viscous media.[11,27,30] This fundamental understanding of ultrasound DSA in both inviscid and viscous media has enabled its use in a myriad of engineering applications, notably manufacturing engineered functional composite materials with tailored properties,[10,11,26,27,31–33] but also manipulating and sorting biological cells in lab-on-a-chip applications,[34–37] performing non-contact particle manipulation for acoustic displays,[23,38,39] and implementing microbubble-aided drug delivery systems,[40] amongst others applications.

However, state-of-the-art theory and experiments limit the assembly of particles into (quasi-) periodic patterns only, because they use single-frequency ultrasound wave fields (see, e.g.,).[18–21,41–44] Consequently, the patterns reflect the periodicity of the ultrasound wave field from which they originate. Furthermore, the complexity of the patterns of particles generally increases with an increasing number of ultrasound transducers because superimposing multiple ultrasound wave fields increases the complexity of the resulting field.[18] Yet, even though theoretically possible, it is often impractical or difficult to increase the number of ultrasound transducers in experiments or engineering applications due to manufacturing tolerances, transducer alignment, and space constraints.[18,20]

Alternative methods to assemble complex patterns of particles based on single-frequency ultrasound wave fields include acoustic holography, in which one spatially modulates the amplitude and/or phase of a single-frequency ultrasound wave field using a 3D printed acoustic kinoform,[45–49] microbubble arrays,[50] or acoustic waveguides that direct acoustic energy into target regions.[51,52] These methods allow assembling particles into complex patterns, but generally display low spatial accuracy and require custom (often 3D printed) hardware for a limited number, or even a single pattern of particles.[53] Moreover, as a result of using custom hardware, the patterns are not reconfigurable in real-time, even though this is often desirable for many engineering applications. Finally, we note that Hou et al.[54] show simulations of symmetric, complex patterns of particles, based on an indirect method that identifies resonance modes within a simulated reservoir filled with a mixture of inviscid liquid and particles. However, they only use frequencies that represent the resonance modes of the reservoir, thus severely limiting the patterns of particles they assemble. Moreover, they do not experimentally validate their method.

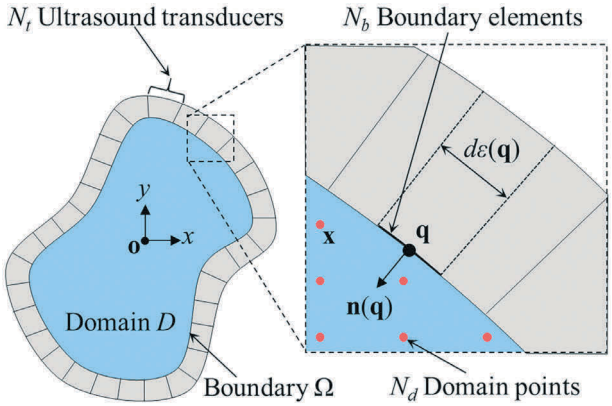

Figure 1. Arbitrary-shaped, 2D fluid reservoir, lined with N_t ultrasound transducers along its boundary Ω. The boundary Ω comprises N_b boundary elements $d\varepsilon(\mathbf{q})$ with normal vector $\mathbf{n}(\mathbf{q})$ at their center $\mathbf{q}$, and it encloses domain D, discretized with N_d domain points.

Thus, the ability to assemble re-configurable, complex patterns of particles with a small number of ultrasound transducers remains a problem. However, it is significant in terms of using ultrasound DSA to, e.g. manufacture functional composite materials with tailored properties that derive their function from the spatial organization and orientation of particles embedded in a matrix, such as electromagnetic metamaterials and (nano)composite materials with tailored structural,[10,12,26] thermal, or electrical properties,[30,55] or with embedded electrical wiring or electromagnetic shielding.[11] Our group has previously demonstrated manufacturing such materials by integrating single-frequency ultrasound DSA with mold casting,[10,26] freeze casting,[12] and vat photopolymerization.[30] Here, we address this problem by introducing multi-frequency instead of single-frequency ultrasound wave fields, and we experimentally demonstrate the assembly of complex patterns of particles, which cannot be assembled with a single-frequency ultrasound wave field. First, we theoretically derive a framework that relates a specific pattern of particles to a multi-frequency ultrasound wave field, generated by any spatial arrangement and number of ultrasound transducers, accounting for the properties of the particles, the fluid medium, and the ultrasound transducers. Second, we experimentally validate the multi-frequency ultrasound DSA theory using a setup with four ultrasound transducers and a multi-frequency ultrasound wave field with two frequency components. Finally, we illustrate the capability of the theory beyond the experimental validation with simulations that demonstrate the assembly of complex, 2D patterns of particles.

2. Results

2.1. Theoretical Model

Figure 1 schematically illustrates the theoretical model, which represents an arbitrary-shaped, 2D fluid reservoir lined with N_t ultrasound transducers along its perimeter. The ultrasound transducers act as ideal piston sources and emit a

multi-frequency ultrasound wave field, which we discretize as $N_f = 64$ uniformly distributed frequencies between 150 kHz $\leq f_j \leq$ 6 MHz. The frequency range derives from practical considerations to implement experiments, such as ultrasound wave attenuation, size of the fluid reservoir, and ultrasound transducer bandwidth.

The reservoir contains an inviscid fluid medium and dispersed compressible spherical particles with radius $r_p << \lambda_s$, with λ_s the smallest wavelength of the multi-frequency ultrasound wave field. We line the reservoir boundary Ω with $1 \leq t \leq N_t$ ultrasound transducers, and discretize it using $N_b \geq N_t$ boundary elements $d\epsilon(\mathbf{q})$, with normal vector $\mathbf{n}(\mathbf{q})$ at their center point $\mathbf{q}$. The boundary Ω encloses the solution domain D, which we discretize using N_d domain points. We compute the ultrasound wave field with frequency f_j in terms of the time-independent, complex scalar velocity potential φ_j. The velocity potential φ_j must satisfy the Helmholtz equation $\nabla^2\varphi_j + k_j{}^2\varphi_j = 0$ in D, where $k_j = 2\pi f_j/c_m$ is the wavenumber of the ultrasound wave field of frequency f_j and c_m is the sound propagation velocity in the fluid medium. Additionally, φ_j must satisfy the impedance boundary condition $\partial\varphi_j/\partial\mathbf{n} + ik_jZ\varphi_j = v_{jt}$ on the portion of the boundary Ω that corresponds to ultrasound transducer t. Here, $i^2 = -1$ and $Z = \rho_m c_m/Z_t$ is the impedance ratio of the fluid medium with density ρ_m and the ultrasound transducers with impedance Z_t, which captures the absorption and reflection of the ultrasound waves at Ω of the solution domain D. We assume constant impedance along Ω, i.e., we maintain Z_t constant for all ultrasound transducers. We let $v_{jt} = V_{jt}\exp(i\theta_{jt})$, where V_{jt} and θ_{jt} denote the amplitude and phase of ultrasound transducer t at frequency f_j. We calculate the velocity potential φ_j using Green's third identity at all points $\mathbf{x}$ in the solution domain for each frequency f_j of the multi-frequency ultrasound wave field as[56,57]

$$\varphi_j(\mathbf{x}) = \Phi(\mathbf{x}) \int_\Omega G_j(\mathbf{q},\mathbf{x})\, v(\mathbf{q})\, d\varepsilon(\mathbf{q}) - \Phi(\mathbf{x}) \int_\Omega \left[ik_jZG_j(\mathbf{q},\mathbf{x}) + \frac{\partial G_j(\mathbf{q},\mathbf{x})}{\partial\mathbf{n}(\mathbf{q})} \right] \varphi_j(\mathbf{q})\, d\varepsilon(\mathbf{q}) \quad (1)$$

Here, $\Phi(\mathbf{x}) = 2$ when $\mathbf{x}$ is on Ω and $\Phi(\mathbf{x}) = 1$ when $\mathbf{x}$ is in D. $d\epsilon(\mathbf{q})$ is the infinitesimally small surface integration element at $\mathbf{q}$ on Ω. $v(\mathbf{q})$ is the complex harmonic velocity amplitude of the ultrasound transducer surface at $\mathbf{q}$, i.e., the right-hand side of the impedance boundary condition. $G_j(\mathbf{q}, \mathbf{x})$ is the Green's function that represents the free ultrasound wave field of frequency f_j, emitted by a point source in $\mathbf{q}$ and evaluated in $\mathbf{x}$, and calculated as[56]

$$G_j(\mathbf{q},\mathbf{x}) = -\frac{i}{4}H_0\left(k_j|\mathbf{q}-\mathbf{x}|\right) \quad (2)$$

H_0 is the 0$^{\text{th}}$ order Hankel function of the first kind and $|\mathbf{q} - \mathbf{x}|$ is the Euclidean distance between $\mathbf{q}$ and $\mathbf{x}$.

We relate the locations where particles assemble to the operating parameters of the ultrasound transducers using the time-averaged acoustic radiation potential (ARP) $U_j(\mathbf{x})$ and the acoustic radiation force $\mathbf{F}_j(\mathbf{x}) = -\nabla U_j(\mathbf{x})$ associated with the velocity potential φ_j of frequency f_j, given as[9,58]

$$U_j(\mathbf{x}) = 2\pi {r_p}^3\rho_m \left\{ \frac{1}{3}{k_j}^2 \left[1 - \left(\frac{\beta_p}{\beta_m} \right)^2 \right] \left|\varphi_j(\mathbf{x})\right|^2 - \left[\frac{\rho_p - \rho_m}{2\rho_p + \rho_m} \right] \left|\nabla\varphi_j(\mathbf{x})\right|^2 \right\} \quad (3)$$

where $\beta_m = 1/(\rho_m {c_m}^2)$ and $\beta_p = 1/(\rho_p {c_p}^2)$ are the compressibility of the fluid medium and particle, respectively. ρ_p is the density and c_p is the sound propagation velocity of the particle.

When a multi-frequency ultrasound wave field exists, the interaction between different frequencies vanishes when averaged over a sufficiently long time (see proof in Supporting Information). Thus, the time-averaged ARP $U(\mathbf{x})$ of a multi-frequency ultrasound wave field at location $\mathbf{x}$ in D is the sum of the ARP $U_j(\mathbf{x})$ for each discrete frequency f_j of the multi-frequency ultrasound wave field, i.e.,

$$U(\mathbf{x}) = \sum_{j=1}^{N_f} U_j(\mathbf{x}) = \sum_{j=1}^{N_f} a_j\left|\varphi_j(\mathbf{x})\right|^2 - b\left|\nabla\varphi_j(\mathbf{x})\right|^2 \quad (4)$$

with

$$a_j = \frac{2}{3}\pi {r_p}^3\rho_m {k_j}^2 \left[1 - \left(\frac{\beta_p}{\beta_m} \right)^2 \right] \quad (5)$$

$$b = 2\pi {r_p}^3\rho_m \left[\frac{\rho_p - \rho_m}{2\rho_p + \rho_m} \right] \quad (6)$$

We use the formulation of Greenhall et al.[18] to calculate $U_j(\mathbf{x})$ for each discrete frequency f_j of the multi-frequency ultrasound wave field as

$$U_j(\mathbf{x}) = {\mathbf{v}_j}^H\mathbf{Q}_j(\mathbf{x})\,\mathbf{v}_j \quad (7)$$

Here, $\mathbf{v}_j = [v_{j1}, ..., v_{jt}, ..., v_{jNt}]^{\mathrm{T}}$ is a vector that contains the operating parameters v_{jt} for each ultrasound transducer $1 \leq t \leq N_t$ and each discrete frequency $1 \leq f_j \leq N_f$. ${\mathbf{v}_j}^H$ is the conjugate transpose of $\mathbf{v}_j$, and the Hermitian matrix $\mathbf{Q}_j(\mathbf{x})$ contains information regarding the velocity potential φ_j (see Equation (1)) as discussed in detail by Greenhall et al.[18] Hence, we compute the time-averaged ARP resulting from a multi-frequency ultrasound wave field as the sum of the time-averaged ARPs for each individual frequency, i.e.,

$$U(\mathbf{x}) = \sum_{j=1}^{N_f} U_j(\mathbf{x}) = \mathbf{v}^H\mathbf{Q}(\mathbf{x})\,\mathbf{v} \quad (8)$$

where $\mathbf{v} = [\mathbf{v}_1, ..., \mathbf{v}_{Nf}]^{\mathrm{T}}$ and contains all vectors $\mathbf{v}_j$ that describe the operating parameters of all ultrasound transducers for each frequency f_j of the multi-frequency ultrasound wave field. $\mathbf{v}^H$ is the conjugate transpose of $\mathbf{v}$, and $\mathbf{Q}(\mathbf{x})$ is a block diagonal Hermitian matrix with $\mathbf{Q}_1(\mathbf{x})$ ... $\mathbf{Q}_j(\mathbf{x})$ ... $\mathbf{Q}_{Nf}(\mathbf{x})$ along its main diagonal.

Particles assemble at the stable points $\mathbf{x}_s$ where the acoustic radiation force $\mathbf{F}(\mathbf{x}) = -\nabla U(\mathbf{x})$ approaches zero and $\mathbf{F}(\mathbf{x})$ points to $\mathbf{x}_s$ in a neighborhood of $\mathbf{x}_s$, which also correspond to the local

minima of the time-averaged ARP with respect to the reservoir coordinates $\mathbf{x}$. Thus, to assemble particles at specific locations $\mathbf{x}_d \in X_d$, we minimize the average ARP $\bar{U}$ at all points $\mathbf{x}_d \in X_d$.

However, rather than solving for the operating parameters of the ultrasound transducers $\mathbf{v}$, we solve for the ultrasound wave field parameters $\mathbf{u}$, i.e., amplitude and phase of each frequency f_j of the multi-frequency ultrasound wave field, since the relationship between $\mathbf{v}$ and $\mathbf{u}$ is not always known a priori, yet can be determined experimentally. Hence,

$$\bar{U} = \mathbf{u}^H \bar{\mathbf{Q}}_C \mathbf{u} \tag{9}$$

where, $\mathbf{u} = [\mathbf{u}_1, \ldots, \mathbf{u}_{Nf}]^T$ contains all vectors $\mathbf{u}_j = [u_{j1}, \ldots, u_{jt}, \ldots, u_{jNt}]^T$ that describe the ultrasound wave field parameters for each ultrasound transducer $1 \leq t \leq N_t$ and each discrete frequency $1 \leq f_j \leq N_f$. The matrix $\bar{\mathbf{Q}}_C$ is given as

$$\bar{\mathbf{Q}}_C = \mathbf{C}^H \bar{\mathbf{Q}} C \tag{10}$$

with $\bar{\mathbf{Q}}$ the average of all matrices $\mathbf{Q}(\mathbf{x}_d)$ for $\mathbf{x}_d \in X_d$, and $\mathbf{C}$ is a matrix that relates the operating parameters of the ultrasound transducers $\mathbf{v}$ to those of the ultrasound wave field $\mathbf{u}$, i.e., $\mathbf{u} = \mathbf{C}\mathbf{v}$, based on the impedance boundary condition. The average ARP $\bar{U}$ must be a real quantity because the matrix $\bar{\mathbf{Q}}_C$ is Hermitian.

Finally, we formulate a constrained quadratic optimization problem to compute the ultrasound wave parameters $\mathbf{u}^*$, required to assemble particles in a specific pattern X_d as

$$\min \bar{U}, \text{subject to } |\mathbf{u}| = 1 \tag{11}$$

We constrain $|\mathbf{u}| = 1$, to represent finite power operation of the ultrasound transducers. The minimum eigenvalue of $\bar{\mathbf{Q}}_C$ (see Equation (9)) and its corresponding eigenvector create the minimum average ARP $\bar{U}$ at all locations $\mathbf{x}_d \in X_d$.

We note that $\bar{\mathbf{Q}}_C$ is a block diagonal matrix that contains information about the velocity potential $\varphi_j(\mathbf{x}_d)$ for $\mathbf{x}_d \in X_d$ of each frequency f_j of the multi-frequency ultrasound wave field. Consequently, there is a basis of eigenvectors where each eigenvector corresponds to a single frequency within the multi-frequency ultrasound wave field. Thus, considering an eigenvector that corresponds to the smallest eigenvalue of $\bar{\mathbf{Q}}_C$ likely limits the resulting ultrasound wave field to a single frequency. To consider a multi-frequency wave field, we calculate a linear combination with unit constants of multiple eigenvectors of $\bar{\mathbf{Q}}_C$ that are within a threshold τ of the smallest eigenvalue γ_{min}, i.e.,

$$\mathbf{u}_\tau = \sum_{\gamma \leq \gamma_{\min} + \tau(\gamma_{\max} - \gamma_{\min})} \mathbf{u}_\gamma \tag{12}$$

Here, $\mathbf{u}_\gamma$ is the eigenvector with eigenvalue γ, and γ_{max} and γ_{min} are the maximum and minimum eigenvalues after eigendecomposition, respectively, and τ is the eigenvector threshold. By construction (see Equation (9)), $\bar{U}$ is the average of the eigenvalues of $\bar{\mathbf{Q}}_C$ in the interval $[\gamma_{min}, \gamma_{min} + \tau(\gamma_{max} - \gamma_{min})]$. We use unit constants in $\mathbf{u}_\tau$ to lend equal importance to each frequency in the multi-frequency ultrasound wave field. However, these constants could be easily adjusted to reflect the frequency response function of realistic ultrasound transducers, and properly weigh the amplitude of each discrete frequency of the multi-frequency ultrasound wave field. The phase of the eigenvectors does not matter when computing $\bar{U}$ if there is at most one eigenvector per frequency. Crucially, it does not affect the locations where particles assemble dictated by Equation (4), under the same assumption. If there are multiple eigenvectors, it may be possible to carry out a secondary optimization, but this is left for future studies, as the approach we present is simpler and yields satisfactory results.

The number of eigenvectors in the linear combination of Equation (12) increases with increasing τ and, thus, the time-averaged ARP of the multi-frequency ultrasound wave field varies with varying τ (see animated visualizations in the Supporting Information). The optimal eigenvector threshold τ^* is unique to each specific pattern of particles X_d (see Supporting Information). We determine τ^* to maximize the ratio of $\bar{U}$ at all locations $\mathbf{x} \notin X_d$ and at $\mathbf{x}_d \in X_d$. Intuitively, this heuristic for choosing τ^* favors $\bar{U}$ that is closer to zero for points belonging to the desired pattern X_d than at the other points. The heuristic may need adjustment if $\bar{U}$ takes negative values. Thus, the unit weight linear combination $\mathbf{u}_\tau$ with τ^* yields the ultrasound wave parameters $\mathbf{u}^*$ required to establish a multi-frequency ultrasound wave field to assemble particles in a specific pattern X_d.

2.2. Experimental Demonstration of Multi-Frequency Ultrasound DSA

Figure 2 shows a 3D schematic (Figure 2a) and a photograph (Figure 2b) of the experimental set-up we use to validate the theoretical model. To perform ultrasound DSA experiments with multi-frequency ultrasound wave fields, we require ultrasound transducers that combine broad bandwidth with high power output. The acoustic radiation force must be of sufficient amplitude to displace particles dispersed in a fluid medium, and simultaneously cover a wide spectrum of frequencies to increase the complexity of the patterns we assemble, and validate the theoretical model. Many ultrasound transducers show broad bandwidth in combination with low power output, which limits the magnitude of the acoustic radiation force and, thus, the ability to drive particles into specific patterns. On the other hand, lead zirconate titanate (PZT) ultrasound transducers typically show high power output, which allows displacing particles dispersed in the fluid medium, but its bandwidth is limited to a narrow region $f \approx f_c$, where f_c is the thickness-mode center frequency of the PZT material. State-of-the-art single-frequency ultrasound DSA methods typically rely on PZT transducers, since bandwidth is not of concern. However, multi-frequency ultrasound DSA ideally requires ultrasound transducers with broad bandwidth and flat frequency response.

Thus, to circumvent the bandwidth versus power tradeoff, we design a stack of two PZT ultrasound transducers with different center frequency, glued together. Figure 2a,b shows magnified inset images of the PZT stack. Furthermore, Figure 2c,d shows carbon microparticles organized in line patterns by energizing a single pair of ultrasound transducers to create a single-frequency ultrasound wave field of $f_1 = 1$ MHz (Figure 2c) and $f_2 = 1.5$ MHz (Figure 2d), respectively. We specifically select these two center frequencies to experimentally demonstrate ultrasound DSA of patterns of particles using a multi-frequency ultrasound wave field with two frequencies and four ultrasound

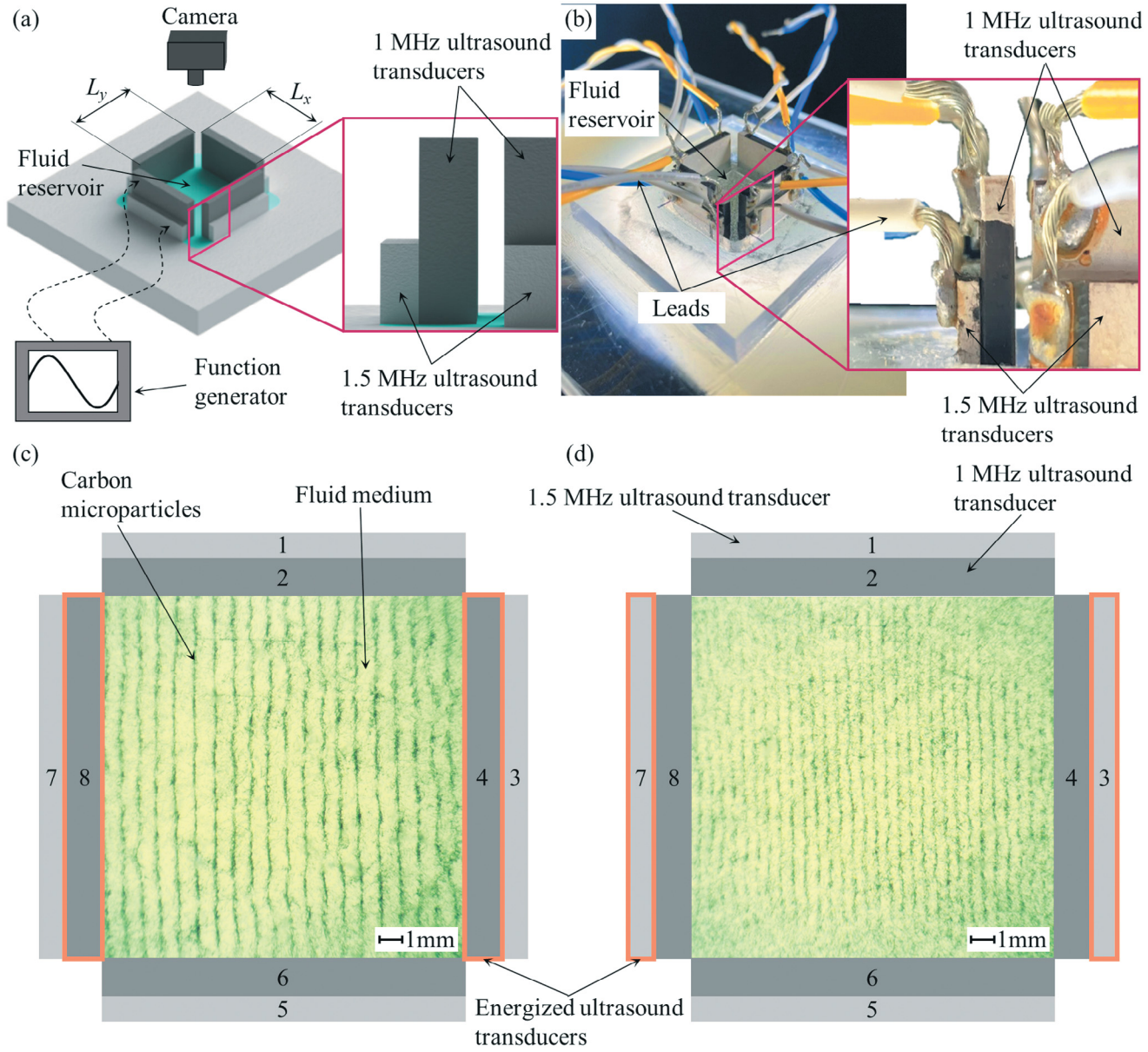

Figure 2. a) Schematic and b) photograph of the experimental setup with carbon microparticles (dark color) dispersed in water (light color), depicting four stacks of two ultrasound transducers with center frequencies $f_1 = 1$ MHz (dark gray) and $f_2 = 1.5$ MHz (light gray), one on each side of the square reservoir. When energizing single transducers (outlined in orange) to create a single-frequency ultrasound wave field, we observe the patterns of particles resulting from c) the 1 MHz ultrasound transducers and d) the 1.5 MHz ultrasound transducers.

transducers, which a single-frequency ultrasound wave field cannot assemble.

Figure 3 shows three selected results that illustrate ultrasound DSA of complex patterns of particles using multi-frequency ultrasound wave fields. The complexity lies in the non-constant distances between the pattern features, which cannot be accomplished with a single-frequency ultrasound wave field. Specifically, we demonstrate organizing complex vertical (Figure 3a) and horizontal (Figure 3b) line patterns, in addition to dot patterns (Figure 3c). Such patterns are relevant to manufacturing functional composite materials with, e.g. structural reinforcement, tailored electrical or thermal conductivity, and with embedded electrical wiring or electromagnetic shielding. The functionality of the patterns of particles of course also depends on the material properties of the particles. However, the ultrasound DSA method, both single- and multi-frequency), works with almost any material type, as long as acoustic contrast exists between the particles and the medium.[9] Furthermore, multi-frequency ultrasound DSA integrates with other materials manufacturing methods, which we have previously demonstrated with single-frequency ultrasound DSA, such as freeze casting,[12,59] mold casting,[10,26] direct ink writing,[33,60] or vat photopolymerization.[11,30] Hence, it enables manufacturing functional composite materials in a layer-by-layer fashion, where in each layer we control the organization

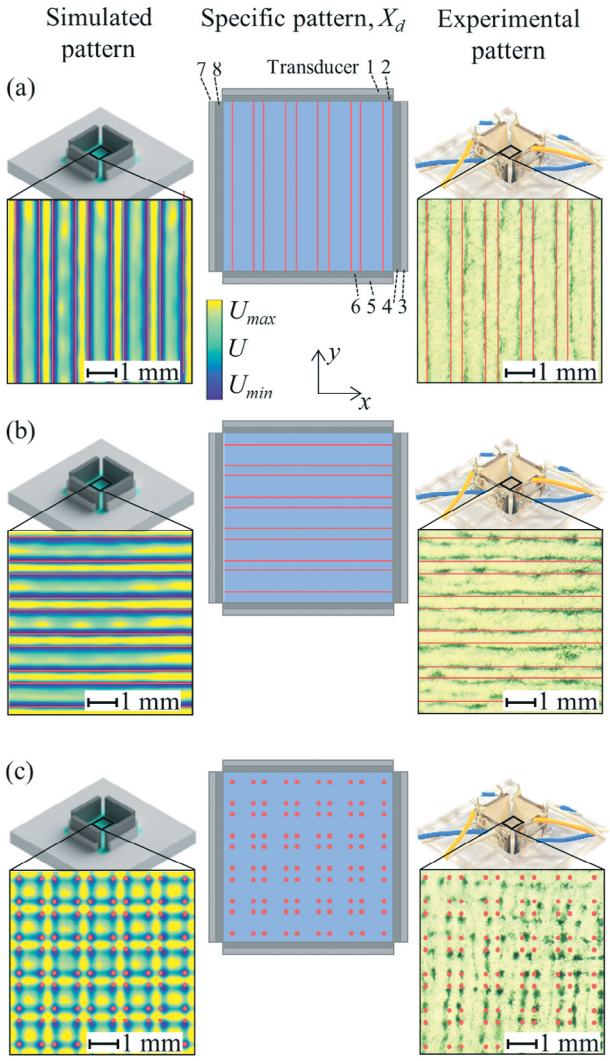

Figure 3. Multi-frequency ultrasound DSA of complex patterns of particles, showing the specific pattern we aim to assemble (center image, red solid lines, and dots), and simulation (left image, time-averaged ARP with blue low and yellow high) and experimental (right image, dark particles, and transparent medium) results for three specific patterns of particles, including a) vertical and b) horizontal line patterns, and (c) dot patterns. The ultrasound transducer numbering corresponds to that of Table 1.

and orientation of the particles, thus enabling tailored functionality.

We schematically depict the specific pattern of particles X_d we aim to assemble (red lines/dots), the simulation results show the time-averaged ARP of the multi-frequency ultrasound wave field (colormap, yellow: max, blue: min), and the experimental results display particles (dark color) that organize in complex patterns in the fluid medium (light color). Both simulations and experiments result from solving the inverse ultrasound DSA problem for a multi-frequency wave field, and applying the resulting ultrasound transducer operating parameters $\mathbf{v}^*$ to the four stacks of two ultrasound transducers (with $f_1 = 1$ MHz and $f_2 = 1.5$ MHz, see Experimental section). **Table 1** summarizes $\mathbf{v}^*$ for the specific

Table 1. $\mathbf{v}^*$ for each result of Figure 3 with multi-frequency ultrasound DSA.

Transducer	Frequency	Vertical lines	Horizontal lines	Dot pattern
1	f_2	0.00	0.48exp(2.87i)	0.32exp(−2.86i)
2	f_1	0.00	0.56exp(−2.63i)	0.38exp(−2.86i)
3	f_2	0.47exp(−2.97i)	0.00	0.31exp(−2.82i)
4	f_1	0.54exp(−2.64i)	0.00	0.38exp(−3.02i)
5	f_2	0.00	0.45exp(−3.06i)	0.36exp(2.70i)
6	f_1	0.00	0.50exp(2.78i)	0.36exp(3.06i)
7	f_2	0.51exp(2.79i)	0.00	0.35exp(2.66i)
8	f_1	0.48exp(2.79i)	0.00	0.38exp(−3.06i)

patterns of particles of Figure 3a,b,c. The ultrasound transducer numbering of Table 1 corresponds to that of Figure 3.

From Figure 3, we qualitatively observe that multi-frequency ultrasound wave fields enable the assembly of complex patterns of particles, which has never been shown before. The three results of Figure 3 also illustrate the underlying physics of multi-frequency ultrasound DSA. It is evident that only two opposing stacks of ultrasound transducers are required to assemble the particles into complex line patterns, whereas all four stacks are needed to assemble the complex dot patterns, similar to single-frequency ultrasound wave fields[18,20] (see also Table 1).

From Figure 3a,b,c, we also determine the pattern error $E_{pat} = 13.7\%$, 14.6%, and 15.9%, and $E_{pat} = 5.3\%$, 6.7%, and 6.0%, between the specific pattern of particles we aim to assemble, and the experimental and theoretical patterns of particles, respectively (see Experimental section). Thus, these results demonstrate experimental validation of the theoretical model. We note that the pattern error of the experimental pattern of particles is approximately double that of the theoretical pattern of particles. However, all pattern errors of the experimental patterns of particles are less than 16%, indicating good agreement between experiment and theory, and similar to pattern errors previously documented for single-frequency ultrasound DSA (see, e.g.).[18,20] Thus, multi-frequency ultrasound DSA does not introduce a penalty in terms of accuracy compared to single-frequency ultrasound DSA.

In addition to the limited bandwidth of ultrasound transducers, the implementation of the experimental setup shows that it is increasingly difficult to physically align and independently control the frequency, amplitude, and phase of an increasing number of (stacks of) ultrasound transducers N_t. Therefore, we limit the experiments to $N_t = 4$ stacks of two ultrasound transducers, which enables the demonstrations of Figure 3, but also limits the complexity of the patterns of particles that we assemble using multi-frequency ultrasound DSA in such a setup.

2.3. Multi-Frequency Ultrasound DSA Simulations of Complex Patterns

To illustrate the capability of the multi-frequency ultrasound DSA method in terms of organizing particles into complex patterns, we use simulations of the validated theoretical model within a square reservoir lined with $N_t = 16$ ultrasound transducers (4 transducers per side), each with $N_f = 64$ uniformly distributed

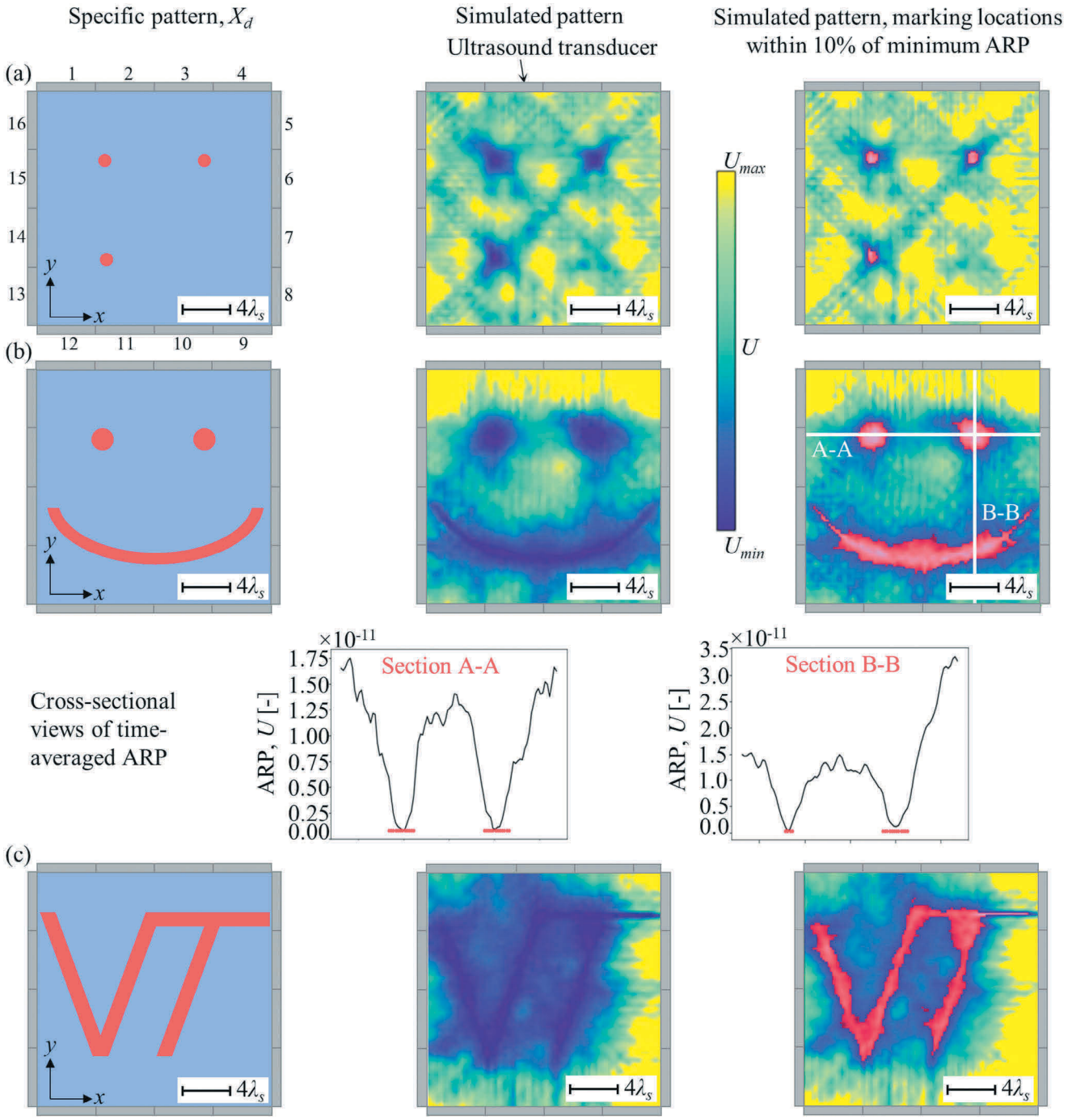

Figure 4. Multi-frequency ultrasound DSA of non-periodic patterns of particles, showing the specific pattern we aim to assemble (left column, red solid lines and dots), the simulated time-averaged ARP with blue low and yellow high), locations within 10% of the minimum ARP where particles assemble (right column, red marked areas), for three specific patterns of particles, including a) a square with a missing vertex, b) a smiley face, and c) the Virginia Tech "VT" logo. Cross-sectional views of the time-averaged ARP illustrate the distinct local minima.

frequencies between 150 kHz $\leq f_j \leq$ 6 MHz. **Figure** 4 shows three examples of organizing complex patterns of particles with multi-frequency ultrasound DSA; a square with a missing vertex (Figure 4a), a smiley face (Figure 4b), and the Virginia Tech "VT" logo (Figure 4c). Similar to Figure 3, we depict the specific pattern of particles X_d we aim to assemble (solid red lines, left column), and the time-averaged ARP (colormap, yellow: max, blue: min, middle column) of the simulated pattern of particles. Particles assemble at the local minima of the ARP (dark blue). To emphasize and visualize the locations where particles assemble, we have marked the areas that are within 10% of the minimum time-averaged ARP in red (right column). Additionally,

for the smiley face (Figure 3b), we show two orthogonal cross-sections of the time-averaged ARP that illustrate the distinct local minimum.

From Figure 4 we observe that multi-frequency ultrasound DSA enables organizing particles into very complex patterns, with just a small number (N_t = 16) of ultrasound transducers. Furthermore, we qualitatively observe good agreement between each of the three specific patterns and the corresponding simulation results, which we emphasize by marking the locations within 10% of the minimum ARP, and the cross-sectional views of the time-averaged ARP. We include the values of the operating parameters of all ultrasound transducers (frequency, amplitude, and phase) for each of the results of Figure 4a–c in the Supporting Information, using the numbering of Figure 4a.

We also quantitatively assess the similarity between the specific patterns of particles and the simulation results using the structural similarity index measure (SSIM), which quantitatively describes the similarity of two images by considering various aspects of human visual perception such as luminance and contrast.[61] We determine SSIM values of 0.94 (Figure 4a), 0.89 (Figure 4b), and 0.82 (Figure 4c), indicating good agreement (spatial accuracy) between the specific patterns of particles we aim to assemble and the simulation results with the multi-frequency ultrasound DSA method.

The optimal simulation result depends on the eigenvector threshold τ, which defines the set of eigenvectors used in the unit weight linear combination $\mathbf{u}_\tau$. The Supporting Information includes animations that show the effect of the eigenvector threshold τ on the simulation result of Figure 4a,b,c. Furthermore, **Figure 5**a,b,c shows the SSIM as a function of eigenvector threshold τ for the three specific patterns of particles of Figure 4a,b,c, with inset images depicting the simulations of the patterns of particles for selected values of eigenvector threshold τ.

From Figure 5, we observe that the maximum SSIM defines the optimal eigenvector threshold τ^* and, correspondingly, the simulated pattern of particles best approaches the specific pattern X_d. The SSIM first increases and then decreases with increasing τ. The number of eigenvectors in the unit weight linear combination $\mathbf{u}_\tau$ increases with increasing τ, which in turn increases the number of frequencies included in the multi-frequency ultrasound wave field. A small τ only includes few eigenvectors and frequencies in the solution, which could prevent local minima of the time-averaged ARP in all locations that correspond to the specific pattern X_d, whereas a large τ could introduce additional local minima beyond those in the locations defined in X_d.

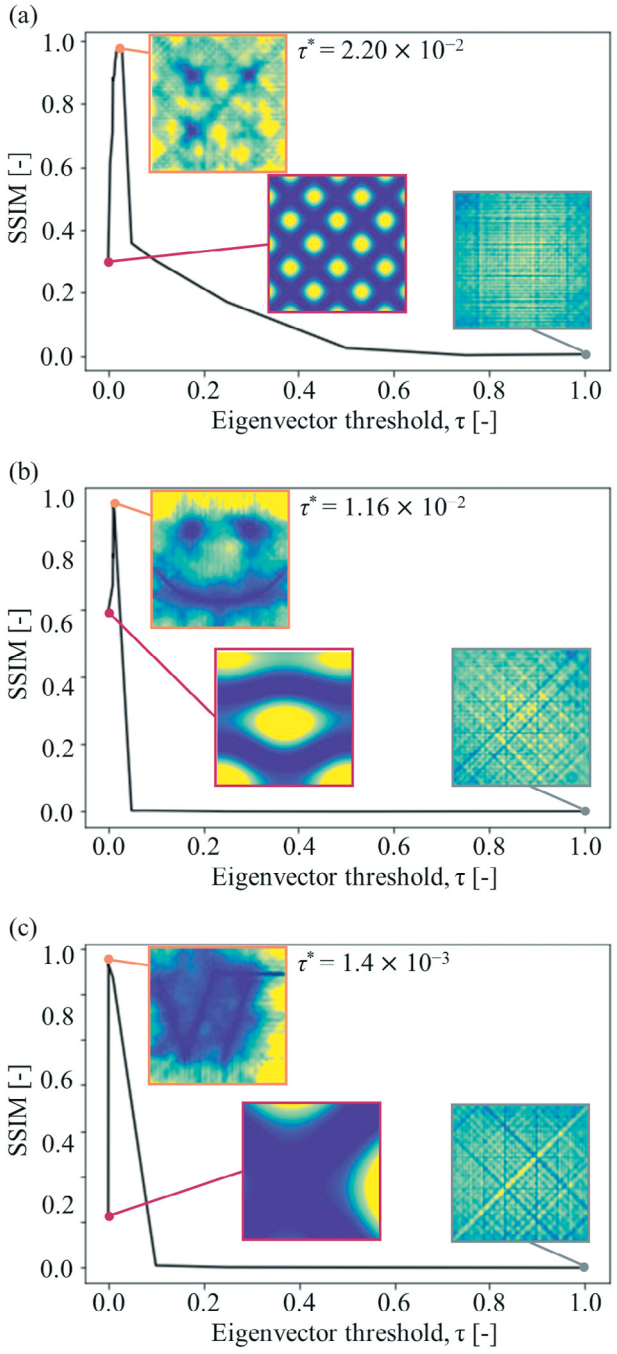

Figure 5. SSIM as a function of the eigenvector threshold τ for the three specific patterns of particles, including a) a square with a missing vertex, b) a smiley face, and c) the Virginia Tech "VT" logo, with inset images depicting the simulations of the patterns of particles for selected values of eigenvector threshold τ.

2.4. Single- Versus Multi-Frequency Ultrasound DSA

To contrast the capability of multi-frequency and single-frequency ultrasound DSA, we simulate the assembly of particles into the Virginia Tech "VT" logo using both methods. **Figure 6** shows the time-averaged ARP (colormap, yellow: max, blue: min) with the specific pattern superimposed (red solid lines). Particles assemble at the local minima of the time-averaged ARP (dark blue locations). Figure 6a shows the simulation results using single-frequency ultrasound DSA using N_t = 1600 ultrasound transducers (f = 1.5 MHz), whereas Figure 6b shows the simulation results using multi-frequency ultrasound DSA and only N_t = 16 ultrasound transducers (150 kHz $\leq f_j \leq$ 6 MHz).

From Figure 6 we qualitatively observe that the multi-frequency ultrasound DSA method approximates the Virginia Tech "VT" logo substantially better than the single-frequency ultrasound DSA method. The Virginia Tech "VT" logo is a

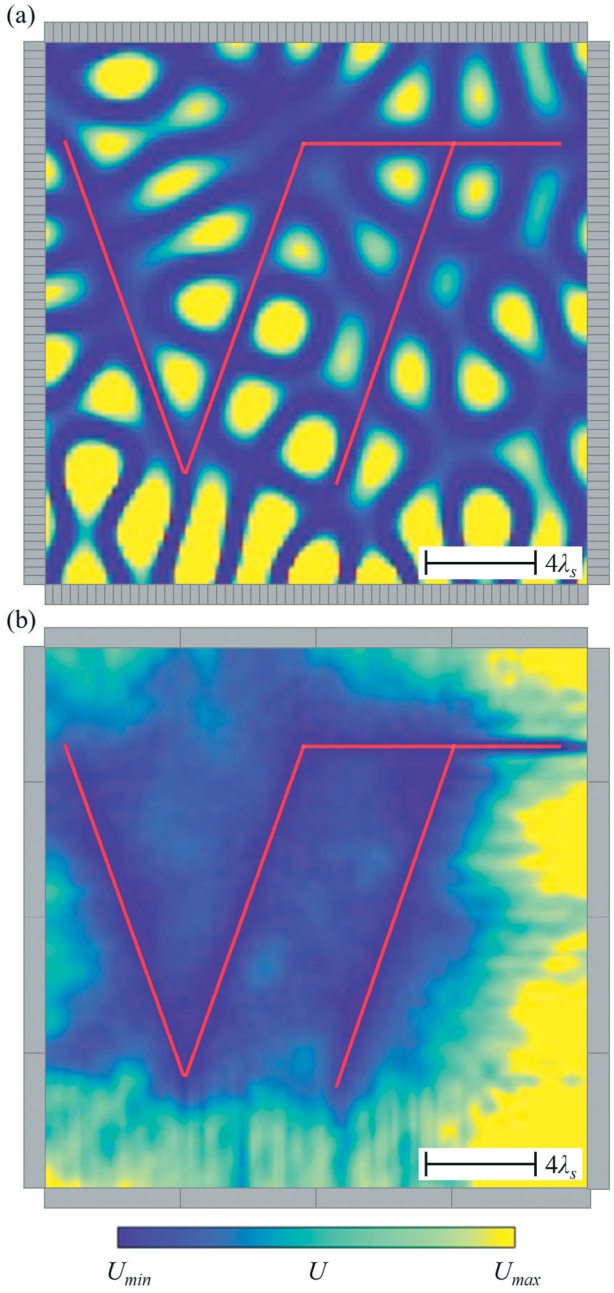

Figure 6. The specific pattern we aim to assemble, Virginia Tech "VT" logo (solid red line), and simulation results showing the pattern of particles using a) single-frequency ultrasound DSA in a square reservoir with $N_t = 1600$ ultrasound transducers and b) multi-frequency ultrasound DSA in a square reservoir with $N_t = 16$ ultrasound transducers.

complex, non-periodic pattern and, thus, single-frequency ultrasound DSA is limited in approximating the pattern with periodic geometric features, even when a large number of ultrasound transducers is available. Furthermore, Figure 6a illustrates that single-frequency ultrasound DSA would not actually assemble the Virginia Tech "VT" logo, because there are many local minima in the time-averaged ARP that are not part of the "VT" logo in addition to those that are part of it, and where particles will also assemble, i.e., they will assemble undesirable additional pattern features in addition to the desired one. In contrast, multi-frequency ultrasound DSA approximates the geometry of the Virginia Tech "VT" logo with remarkable accuracy using just 16 ultrasound transducers, owing to its ability to assemble complex patterns of particles without introducing undesirable additional pattern features. We also quantify the SSIM = 0.31 (single-frequency ultrasound DSA) and SSIM = 0.82 (multi-frequency ultrasound DSA) for both simulation results, confirming the qualitative observations.

3. Discussion

The results of this work provide a theoretical framework that relates any specific pattern of particles to any multi-frequency ultrasound wave field, for any spatial arrangement and number of ultrasound transducers, accounting for the properties of the particles, the medium, and the ultrasound transducers. It enables the experimental assembly of complex patterns that are reconfigurable and do not require an impractical number of ultrasound transducers, which is needed with single-frequency ultrasound wave fields. Furthermore, it does not require custom hardware for each different pattern, which is needed with acoustic holography.

We note that the theoretical model accounts for single scattering only, and does not account for interparticle forces, which is a simplification that we justify based on the size of the particles in our experiments, for which the interparticle forces are substantially smaller than the primary acoustic radiation force. However, the particle interaction forces become increasingly important with decreasing particle size and, thus, one may need to account for interaction forces, e.g. when using nano- instead of microparticles.

The theoretical model also relies on Rayleigh scattering, i.e., it assumes that the size of the particles is small compared to the wavelength of the ultrasound wave field. In the context of a multi-frequency ultrasound wave field this refers to the shortest wavelength, i.e., the highest frequency component of the wave field. Hence, the introduction of multi-frequency ultrasound wave fields also offers advantages in terms of accuracy and resolution compared to single-frequency wave fields. The spatial resolution of ultrasound DSA is limited to a half wavelength because local minima of the ARP correspond to nodes or antinodes of the standing ultrasound wave. Thus, when using single-frequency ultrasound wave fields, the resolution is fixed by the choice of the frequency. However, the choice of frequency also needs to accommodate the other pattern features one intends to assemble. When using multi-frequency wave fields, we leverage low-frequency components to create pattern features with large distances between them, and high-frequency components to obtain high-resolution pattern features.

The pattern error of the experimental results originates from imperfections in the experimental setup, which includes manufacturing tolerances of the acrylic reservoir that affect the alignment of the ultrasound transducers with respect to each other and the reservoir boundary. Additionally, we create the stack of ultrasound transducers by manually gluing two PZT plates with different center frequency together, which again introduces alignment error and a thin layer of glue that acts

as a soft spring between the two hard PZT plates. As a result, we measure slight variability of the center frequencies of the individual PZT plates in each stack. We confirm the effect of ultrasound transducer alignment on the pattern error by manufacturing several reservoirs, with different transducer stacks, and observed repeatable pattern errors. In contrast, the theoretical model assumes perfect reservoir geometry and alignment of the ultrasound transducers, and constant center frequencies of the PZT plates between different stacks. Furthermore, the theoretical model assumes that the ultrasound transducers act as ideal piston sources, which is unlikely in the experiment as we solder leads to the surfaces of the PZT plates, which locally adds mass and, thus, causes them to deviate from an ideal piston source. The use of commercial phased-arrays could potentially solve the problem of aligning several ultrasound transducers with each other, but also substantially increases cost and complexity, compared to the bench-top system we implemented in the lab. Alternatively, performing ultrasound DSA in air as opposed to liquids would enable using ultrasound transducers optimized for gases, which typically show a broader bandwidth than those optimized for liquids[21,23,25] and, thus, would benefit multi-frequency ultrasound DSA. However, ultrasound transducers for use in air also typically show a lower center frequency than those for liquids, which increases the wavelength, and reduces the spatial resolution of the patterns of particles. Additionally, one needs to levitate the particles in the air, which limits the particle type (weight) and the number of particles. Finally, we chose to do the experiments in liquids because the results translate directly to low-viscosity resins and photopolymers for the manufacturing of functional materials, which is the context of this work.

We also note that even though we sonicate the mixture of water and carbon microparticles, their spatial distribution in the fluid medium is not perfectly uniform, even though the theoretical model adopts that assumption. Additionally, the experiments in this work use water and carbon microparticles, but we emphasize that ultrasound DSA (both single- and multi-frequency) works with almost any material type as long as acoustic contrast exists between the particles and the medium. However, the magnitude of the acoustic radiation force depends on the material properties of the particles (and medium), and the drag force that acts on the particles depends on the viscosity and density of the medium, and the size of the particles. Thus, the material choice affects the velocity by which particles organize and orient into patterns. This work shows experiments and simulations with spherical particles, but we note that the results also translate to high aspect ratio particles, as we have shown previously for single-frequency ultrasound DSA.[24] However, high aspect ratio particles require considering both spatial organization and orientation of the particles, whereas spherical particles only require organization because they are axisymmetric.

The pattern error of the simulated pattern of particles results from the fundamental limitations of the theory, i.e., we limit the number of frequencies $N_f = 64$ in the multi-frequency ultrasound wave field, the number of boundary elements $N_b = 400$, and number of domain points $N_d = 10000$ (spatial resolution $\sigma_x = L_x/100 = 0.18$ mm and $\sigma_y = L_y/100 = 0.18$ mm) to limit computational cost. Also, the theoretical model only considers single wave scattering, even though accounting for multiple wave scattering and secondary acoustic radiation forces[62] could further improve the accuracy of the simulations, in particular, because of the local close-packing of particles within the pattern features that result from ultrasound DSA.[63] Thus, the physical imperfections of the experimental setup explain that the pattern error of the theoretical compared to the experimental pattern of particles is substantially smaller.

4. Conclusion

Based on the experiments and simulations we conclude that multi-frequency ultrasound DSA substantially improves upon state-of-the-art single-frequency ultrasound DSA methods that can only assemble simple, periodic patterns of particles, or require an impractically large number of ultrasound transducers to assemble complex patterns.

Specifically, 1) the acoustic radiation force associated with multi-frequency ultrasound wave fields enables the assembly of complex patterns of particles that are not possible with single-frequency ultrasound wave fields. Moreover, the accuracy of the assembly of specific patterns with multi-frequency ultrasound DSA is similar to that of single-frequency ultrasound DSA. 2) Multi-frequency ultrasound DSA enables the assembly of complex, 2D patterns of particles with substantially fewer ultrasound transducers than when using a single-frequency ultrasound wave field, if it is even possible to assemble the specific pattern with the latter method. The complexity of the patterns of particles increases with increasing number of ultrasound transducers, which is valid for both single- and multi-frequency ultrasound DSA, and with increasing number of frequencies in the multi-frequency ultrasound wave field. Notably, multi-frequency ultrasound DSA results in far fewer undesirable pattern features that result from wave interference than single-frequency ultrasound DSA. 3) Multi-frequency ultrasound DSA enables the assembly of complex patterns of particles without the need for custom hardware, i.e., it offers reconfigurability.

Hence, this new knowledge enables substantially expanding the patterns of particles that ultrasound DSA can assemble, which is important in the context of manufacturing functional polymer matrix composite materials that derive their functionality from the spatial arrangement of particles (filler) in a matrix material.

5. Experimental Section

Experimental Set-Up and Materials: The setup comprised a square methyl methacrylate (plexiglass) reservoir with internal dimensions $L_x = L_y = 18$ mm, selected to balance the attenuation of the highest frequency and the near-field of the lowest frequency of the multi-frequency ultrasound wave field. The acrylic reservoir contained a mixture of water ($\rho_m = 998$ kg m^{-3}, $c_m = 1482$ m s^{-1})[64] and a 0.75% volume fraction of dispersed carbon microparticles (Zoltek PX30 MF150, $r_p = 3.6$ µm, $\rho_p = 1750$ kg m^{-3}, $c_m = 2000$ m s^{-1}),[65] under standard temperature and pressure. The combination of ultrasound transducers ($Z_t = 33$ MPa s m^{-1})[66] and fluid medium created a hard acoustic boundary with $Z = 0.045$.

Ultrasound Transducers: Two different PZT transducers were used, one with $f_1 = 1$ MHz (Steminc, Florida, USA), and another one with $f_2 = 1.5$ MHz (American Piezo, Pennsylvania, USA), glued together with a thin layer of superglue (Loctite, Ohio, USA), and mounted to each side of the square reservoir. The full-width half maximum of the ultrasound

transducers spanned 950 kHz–1.2 MHz and 1.5 MHz–1.7 MHz, respectively. An arbitrary function generator (Tektronix AFG3102, Oregon, USA) energized each ultrasound transducer, and supplies an arbitrary waveform that was the superposition of the single-frequency ultrasound waves at their respective amplitude and phase, which constituted the multi-frequency ultrasound wave field that results from solving the inverse multi-frequency ultrasound DSA problem.

Experimental Validation Methodology: First, a specific pattern of particles X_d in a square reservoir lined with $N_t = 4$ stacks of ultrasound transducers ($f_1 = 1$ MHz and $f_2 = 1.5$ MHz) that contains water with dispersed carbon microfibers was defined. Then,the ultrasound wave parameters $\mathbf{u}^*$ required to assemble the specific pattern of particles X_d by solving the inverse multi-frequency ultrasound DSA problem and converting $\mathbf{u}^*$ to the operating parameters of the stacks of ultrasound transducers $\mathbf{v}^*$ were calculated. Subsequently, $\mathbf{v}^*$ to both the theoretical model and the experimental setup to obtain a theoretical prediction and experimental observation of the resulting pattern of particles was applied. The local minima of the time-averaged ARP visualized the simulated organization of particles in a specific pattern, whereas an optical microscope was used with a digital camera (80X magnification, AmScope, California, USA) to observe and record the experimental result.

Quantitative Pattern Assessment: The average pattern error E_{pat}, similar to what others have described previously,[18,20,21,67] to quantify the similarity between the experimental and theoretical results was determined. The pattern error was the average distance between the centroids of the specific pattern of particles $X_{d,}$ it was aimed to assemble, and either the theoretical or experimentally obtained pattern of particles, normalized by the smallest nominal pattern spacing $\lambda_s/2$, which was half the wavelength of the largest frequency of the multi-frequency ultrasound wave field. The similarity between the specific patterns of particles and the simulation results using the structural similarity index measure (SSIM), by binarizing the time-averaged ARP was quantitatively assessed, taking into account local color intensity variations using the adaptive minimum binary threshold method,[68,69] and defining the specific pattern of particles, it was aimed to assemble as $\mathbf{x}_d \in X_d = 1$ and $\mathbf{x} \notin X_d = 0$.

Supporting Information

Supporting Information is available from the Wiley Online Library or from the author.

Acknowledgements

C.T.P. and B.R. acknowledge support from the National Science Foundation under award CMMI-2246277. C.T.P. also acknowledges support from the Department of Defense National Defense Science and Engineering Graduate Fellowship program. F.G.V. acknowledges support from the National Science Foundation under awards DMS-2008610 and DMS-2136198. Finally, the authors acknowledge Advanced Research Computing at Virginia Tech for providing computational resources and technical support that have contributed to the results reported within this paper. URL: https://arc.vt.edu/. Note that portions of this work are part of the MS thesis of C.T.P. The VT logo contained herein is a registered trademark of Virginia Polytechnic Institute and State University (Virginia Tech).

Conflict of Interest

The authors declare no conflict of interest.

Data Availability Statement

The data that support the findings of this study are available from the corresponding author upon reasonable request.

Keywords

engineered composite materials, manufacturing, multi-frequency wave field, ultrasound-directed self-assembly

Received: January 4, 2024
Revised: March 21, 2024
Published online:

[1] M. Grzelczak, J. Vermant, E. M. Furst, L. M. Liz-Marzán, *ACS Nano* **2010**, *4*, 3591.
[2] K. D. Barbee, A. P. Hsiao, M. J. Heller, X. Huang, *Lab Chip* **2009**, *9*, 3268.
[3] J. B. Tracy, T. M. Crawford, *MRS Bull.* **2013**, *38*, 915.
[4] B. W. Drinkwater, *Lab Chip* **2016**, *16*, 2360.
[5] P. V. Kamat, K. G. Thomas, S. Barazzouk, G. Girishkumar, K. Vinodgopal, D. Meisel, *J. Am. Chem. Soc.* **2004**, *126*, 10757.
[6] M. Fujiwara, E. Oki, M. Hamada, Y. Tanimoto, I. Mukouda, Y. Shimomura, *J. Phys. Chem. A* **2001**, *105*, 4383.
[7] B. Liu, S. Liu, V. Devaraj, Y. Yin, Y. Zhang, J. Ai, Y. Han, J. Feng, *Nat. Commun.* **2023**, *14*, 4920.
[8] X. Chen, R. E. Apfel, *J Acoust Soc Am* **1996**, *99*, 713.
[9] L. P. Gor'kov, *Sov. Phys. Dokl.* **1962**, *6*, 773.
[10] M. D. Haslam, B. Raeymaekers, *Compos. Part B Eng.* **2014**, *60*, 91.
[11] K. Niendorf, B. Raeymaekers, *Compos. Part B Eng.* **2021**, *223*, 109096.
[12] M. Mroz, J. L. Rosenberg, C. Acevedo, J. J. Kruzic, B. Raeymaekers, S. E. Naleway, *Materialia* **2020**, *12*, 100754.
[13] L. E. Kinsler, A. R. Frey, A. B. Coppens, J. V. Sanders, *Fundamentals of Acoustics*, John Wiley & Sons, New Jersey, United States **2000**.
[14] L. V. King, *Proc. R. Soc. Lond. Ser. – Math. Phys. Sci.* **1934**, *147*, 212.
[15] K. Yosioka, Y. Kawasima, *Acta Acust. United Acust.* **1955**, *5*, 167.
[16] J. Greenhall, F. G. Vasquez, B. Raeymaekers, *Appl. Phys. Lett.* **2013**, *103*, 074103.
[17] A. L. Bernassau, C. R. P. Courtney, J. Beeley, B. W. Drinkwater, D. R. S. Cumming, *Appl. Phys. Lett.* **2013**, *102*, 164101.
[18] J. Greenhall, F. G. Vasquez, B. Raeymaekers, *Appl. Phys. Lett.* **2016**, *108*, 103103.
[19] C. R. P. Courtney, C.-K. Ong, B. W. Drinkwater, A. L. Bernassau, P. D. Wilcox, D. R. S. Cumming, *Proc. R. Soc. Math. Phys. Eng. Sci.* **2011**, *468*, 337.
[20] M. Prisbrey, J. Greenhall, F. G. Vasquez, B. Raeymaekers, *J. Appl. Phys.* **2017**, *121*, 014302.
[21] M. Prisbrey, B. Raeymaekers, *Phys. Rev. Appl.* **2018**, *10*, 034066.
[22] Y. Ochiai, T. Hoshi, J. Rekimoto, *PLoS One* **2014**, *9*, e97590.
[23] A. Marzo, S. A. Seah, B. W. Drinkwater, D. R. Sahoo, B. Long, S. Subramanian, *Nat. Commun.* **2015**, *6*, 8661.
[24] M. Prisbrey, B. Raeymaekers, *Phys. Rev. Appl.* **2019**, *12*, 014014.
[25] M. Prisbrey, F. G. Vasquez, B. Raeymaekers, *Phys. Rev. Appl.* **2020**, *14*, 024026.
[26] J. Greenhall, L. Homel, B. Raeymaekers, *J. Compos. Mater.* **2019**, *53*, 1329.
[27] M.-S. Scholz, B. W. Drinkwater, R. S. Trask, *Ultrasonics* **2014**, *54*, 1015.
[28] M. Settnes, H. Bruus, *Phys Rev E* **2012**, *85*, 016327.
[29] S. Noparast, F. G. Vasquez, B. Raeymaekers, *J. Appl. Phys.* **2022**, *131*, 134901.
[30] J. Greenhall, B. Raeymaekers, *Adv. Mater. Technol.* **2017**, *2*, 1700122.
[31] X. Li, K. M. Lim, W. Zhai, *Appl. Mater. Today* **2022**, *26*, 101388.
[32] S. J. Petersen, S. Basu, B. Raeymaekers, M. Francoeur, *J Quant Spectrosc Radiat Transf* **2013**, *129*, 277.
[33] P. Wadsworth, I. Nelson, D. L. Porter, B. Raeymaekers, S. E. Naleway, *Mater. Des.* **2020**, *185*, 108243.

[34] H. Mulvana, S. Cochran, M. Hill, *Adv. Drug Delivery Rev.* **2013**, *65*, 1600.
[35] T. Laurell, F. Petersson, A. Nilsson, *Chem. Soc. Rev.* **2007**, *36*, 492.
[36] L. Johansson, F. Nikolajeff, S. Johansson, S. Thorslund, *Anal. Chem.* **2009**, *81*, 5188.
[37] D.-H. Kim, A. Haake, Y. Sun, A. P. Neild, J.-E. Ihm, J. Dual, J. A. Hubbell, B.-K. Ju, B. J. Nelson, in *26th Anniversary International Conference on IEEE Engineering and Medical Biology Societies*, IEEE, San Francisco, CA, USA, **2004**, pp. 2571–2574.
[38] T. Kozuka, K. Yasui, T. Tuziuti, A. Towata, Y. Iida, *Jpn. J. Appl. Phys.* **2007**, *46*, 4948.
[39] R. Hirayama, D. Martinez Plasencia, N. Masuda, S. Subramanian, *Nature* **2019**, *575*, 320.
[40] Y. Yamakoshi, N. Nakajima, T. Miwa, *Jpn. J. Appl. Phys.* **2007**, *46*, 4847.
[41] B. Raeymaekers, C. Pantea, D. N. Sinha, *J. Appl. Phys.* **2011**, *109*, 014317.
[42] C. R. P. Courtney, C.-K. Ong, B. W. Drinkwater, P. D. Wilcox, in 2011 IEEE Int. Ultrason. Symp. IEEE, Orlando, FL, USA **2011**, pp. 192.
[43] C. R. P. Courtney, C. E. M. Demore, H. Wu, A. Grinenko, P. D. Wilcox, S. Cochran, B. W. Drinkwater, *Appl. Phys. Lett.* **2014**, *104*, 154103.
[44] M.-S. Scholz, B. W. Drinkwater, T. M. Llewellyn-Jones, R. S. Trask, *IEEE Trans. Ultrason. Ferroelectr. Frequation Control* **2015**, *62*, 1845.
[45] K. Melde, A. G. Mark, T. Qiu, P. Fischer, *Nature* **2016**, *537*, 518.
[46] K. Melde, E. Choi, Z. Wu, S. Palagi, T. Qiu, P. Fischer, *Adv. Mater.* **2018**, *30*, 1704507.
[47] Z. Ma, A. W. Holle, K. Melde, T. Qiu, K. Poeppel, V. M. Kadiri, P. Fischer, *Adv. Mater.* **2020**, *32*, 1904181.
[48] Y. Gu, C. Chen, J. Rufo, C. Shen, Z. Wang, P.-H. Huang, H. Fu, P. Zhang, S. A. Cummer, Z. Tian, T. J. Huang, *ACS Nano* **2020**, *14*, 14635.
[49] Y. Xie, C. Shen, W. Wang, J. Li, D. Suo, B.-I. Popa, Y. Jing, S. A. Cummer, *Sci. Rep.* **2016**, *6*, 35437.
[50] Z. Ma, K. Melde, A. G. Athanassiadis, M. Schau, H. Richter, T. Qiu, P. Fischer, *Nat. Commun.* **2020**, *11*, 4537.
[51] Y. Bian, F. Guo, S. Yang, Z. Mao, H. Bachman, S.-Y. Tang, L. Ren, B. Zhang, J. Gong, X. Guo, T. J. Huang, *Microfluid Nanofluidics* **2017**, *21*, 132.
[52] K.-W. Tung, P.-S. Chung, C. Wu, T. Man, S. Tiwari, B. Wu, Y.-F. Chou, F. Yang, P.-Y. Chiou, *Lab Chip* **2019**, *19*, 3714.
[53] M. D. Brown, B. T. Cox, B. E. Treeby, *Appl. Phys. Lett.* **2017**, *111*, 244101.
[54] Z. Hou, J. Li, Z. Zhou, Y. Pei, *Int J Mech Sci* **2022**, *222*, 107232.
[55] K. Niendorf, B. Raeymaekers, *Compos. Part Appl. Sci. Manuf.* **2020**, *129*, 105713.
[56] L. C. Wrobel, *The Boundary Element Method: Applications in Thermo-Fluids and Acoustics*, John Wiley & Sons, Hoboken, New Jersey, United States **2002**, Vol. *1*.
[57] S. Chandler-Wilde, S. Langdon, **2007**, *SIAM J. Numer. Anal.*, *45*, 610
[58] M. Barmatz, P. Collas, *J Acoust Soc Am* **1985**, *77*, 928.
[59] T. A. Ogden, M. Prisbrey, I. Nelson, B. Raeymaekers, S. E. Naleway, *Mater. Des.* **2019**, *164*, 107561.
[60] A. Felt, B. Raeymaekers, *Addit. Manuf. Lett.* **2023**, *5*, 100120.
[61] Z. Wang, A. C. Bovik, H. R. Sheikh, E. P. Simoncelli, *IEEE Trans Image Process* **2004**, *13*, 600.
[62] V. F. K. Bjerknes, *Fields of Force: A Course of Lectures in Mathematical Physics Delivered December 1 to 23, 1905*, Columbia University Press, New York, **1906**.
[63] S. Zhang, C. Qiu, M. Wang, M. Ke, Z. Liu, *New J Phys* **2016**, *18*, 113034.
[64] W. M. Haynes, D. R. Lide, T. J. Bruno, *CRC Handbook of Chemistry and Physics*, CRC Press, Boca Raton, **2014**.
[65] Zoltek Corporation, Website: https://zoltek.com/products/px30/ (accessed: March 2024).
[66] Y. Wang, J. Tao, F. Guo, S. Li, X. Huang, J. Dong, W. Cao, *Sensors* **2018**, *18*, 4424.
[67] M. Prisbrey, F. G. Vasquez, B. Raeymaekers, *Appl. Phys. Lett.* **2020**, *117*, 111904.
[68] J. M. Prewitt, M. L. Mendelsohn, *Ann. N. Y. Acad. Sci.* **1966**, *128*, 1035.
[69] C. A. Glasbey, *CVGIP Graph. Models Image Process.* **1993**, *55*, 532.